Supplement of Biogeosciences, 23, 6491–6520, 2026
https://doi.org/10.5194/bg-23-6491-2026-supplement

Biogeosciences
Open Access

Supplement of

How beech ecophysiology shapes temperate forest gross primary productivity – Part 2: Identifying critical timeframes across phenological stages

Jonathan Bitton et al.

Correspondence to: Jonathan Bitton (jonathan.bitton@uliege.be)

Supplementary material

Supplement S1: Synthesis of corrections and choices when computing fluxes and drivers

1. Data

We used 24 years (1997–2020) of half-hourly eddy-covariance and meteorological measurements from the ICOS forest ecosystem station FR-Hes, located in a beech-dominated temperate forest. During the study period, fluxes were acquired successively from three tower configurations with measurement heights of 18 m (1997–1999), 23.34 m (2000–2012), and 27.1 m (2013–2020). Footprint analyses consistently showed that at least 80 % of the measured flux originated from the beech-dominated area of the forest, ensuring temporal comparability across tower configurations.

2. Quality control filtering

We applied all quality flags generated during eddy-covariance processing to ensure that only reliable turbulent fluxes were retained. Half-hours failing either stationarity or integral turbulence characteristics tests were discarded for the affected variables, specifically: CO_2 flux (FC), and associated net ecosystem exchange (NEE) estimates, latent heat (LE), and sensible heat (H). In addition, several short periods influenced by snow cover or instrumentation issues were manually excluded based on site operator documentation.

3. Backup measurements

Missing meteorological variables were reconstructed using adaptive windowed linear regression between co-located sensors measuring the same quantity. For each missing value, a linear regression was fitted within a moving window centered on the gap, beginning with 7 d and expanding in 7 d increments up to a maximum window length. A regression was accepted only when:

- at least 5 d of valid data and at least one-third of window values were available,
- the predicted value did not require substantial extrapolation,
- the regression achieved $R^2 \geq 0.8$.

This procedure was applied to variables with redundant sensors (e.g., air temperature, humidity, radiation, precipitation).

4. CO_2 storage flux

The below-canopy CO_2 storage flux (SC) was computed from vertical CO_2 concentration profiles measured within the canopy and trunk space. For each height level i, temporal CO_2 changes were estimated as half-hour finite differences (dC_i/dt). The vertically integrated storage term was calculated as:

$$\mathrm{SC} = \rho \sum_i \frac{dC_i}{dt} \Delta z_i$$

where Δz_i is the thickness of the layer represented by level i, derived from the midpoints between consecutive heights, and ρ is the air molar density. When the highest profile measurement was missing, the CO_2 concentration at the eddy-covariance sampling height was used as a substitute for the uppermost layer. To maximize temporal coverage, storage was additionally computed for incomplete profiles when at least four profile points were available, with layer thicknesses recalculated using the subset of available heights.

To fill remaining gaps, we used a turbulence- and season-dependent lookup table (Aubinet et al., 2018). Storage values were grouped by 0.1 m s^{-1} friction velocity (u^*) classes, month, and half-hour of day, and missing values were replaced by the corresponding class mean. Final NEE was calculated as NEE = FC + SC. After this procedure, 10.8 % of NEE values were missing.

5. u^* threshold estimation and filtering

Periods of insufficient turbulence were identified using a year-wise and seasonally resolved u^* approach. Two seasons were defined based on the site's climatology:

- Growing season (GS): May–September,
- Dormant season: October–April.

A two-season scheme was preferred over a four-season partition because winter periods yielded poorly constrained and spuriously high u^* thresholds.

For each year × season combination, a bootstrap distribution of u^* thresholds was derived, and the median was retained for all subsequent analyses. NEE and H observations were restricted to periods with u^* above this threshold. LE was not u^*-filtered, as nighttime LE is typically close to zero and insensitive to u^*. Following u^* filtering, 22.9 % of NEE values were missing overall (21.5 % during GS, 23.9 % during the dormant season; 10.9 % during daytime, 35 % during nighttime).

6. MDS gapfilling of fluxes and meteorological variables

Remaining gaps in NEE, H, LE, and all meteorological drivers (air temperature, incoming solar radiation, vapor pressure deficit) were filled using the standard marginal distribution sampling (MDS) approach implemented in REddyProc (Wutzler et al., 2018). MDS relies on hierarchical selection of donor values under similar meteorological conditions, expanding the temporal window as necessary. Outlier detection was not applied to NEE, as tests with additional filters (value thresholds, second-derivative tests) showed negligible influence on final indicator values and tended to remove high-magnitude uptake events disproportionately. Nonetheless, spikes in high frequency data were already filtered upstream in the station's EC processing.

7. Partitioning

Gross primary production and ecosystem respiration were partitioned from NEE using the nighttime-based flux partitioning algorithm in REddyProc, applied independently for each year. This year-wise approach accounts for the long-term evolution of ecosystem respiration associated with forest maturation. Nighttime partitioning was preferred to daytime partitioning since it minimizes assumptions about GPP response functions and avoids introducing additional model dependencies.

Supplement S2: Allometric relationships for biomass estimation at FR-Hes

Tree biomass was estimated from circumference measurements using site-specific allometric relationships developed for the Hesse forest (Le Goff and Ottorini, 2001), later revised by Ottorini (2012, unpublished dataset). These relationships are based on destructive sampling of 21 beech trees spanning different canopy strata and size classes.

Total (B), aboveground (B_{above}) and belowground (B_{below}) biomass (in kg) were estimated according to:

$$B = 0.0165 \cdot circ^{2.32}$$

$$B_{above} = 0.156 \cdot circ^{2.29}$$

$$B_{below} = B - B_{above}$$

where circ is tree circumference (cm).

These relationships followed power-law formulations and showed strong statistical support, with highly significant coefficients (p-values < 0.001) and low residual errors (Fig. S2).

The relationships were originally calibrated for trees with circumference up to approx. 70 cm. In the present dataset, a limited proportion of trees (about 14 % in 2021) exceeded this range. However, comparison with alternative site-specific allometric equations (Le Goff and Ottorini, 2001; Bernard Longdoz, personal communication, 2024) as well as equations available for beech in the GlobAllomeTree database (Henry et al., 2013) showed differences within approx. 10 %, supporting the use of these relationships over the full dataset.

These equations were therefore considered appropriate for estimating biomass dynamics at the stand level for the purposes of this study.

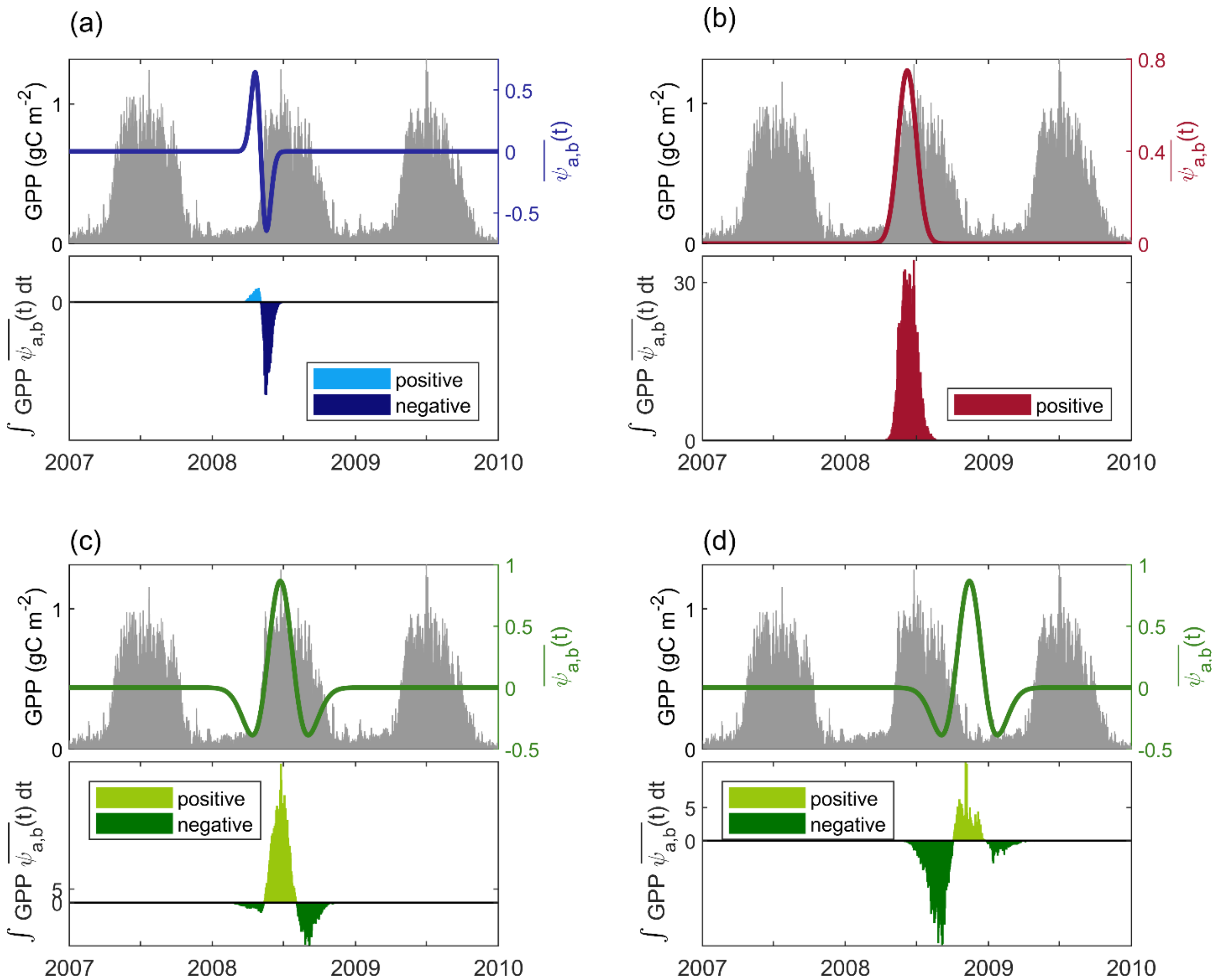

Figure S1: Computation steps for deriving (a) IRise, expressed as the DOG1 April peak at a 3-month period on a normalized GPP signal, (b) IPeak, computed using the opposite of the right lobe of the DOG1 April peak, which is equivalent to a Gaussian function, at a 7-month period, and (c-d) IDrop, defined as the ratio of the DOG2 (c) June to (d) November peaks at 6-month periods. For each panel, the top graph displays the wavelet at selected scale and time with the GPP signal in the background (restricted to positive values for readability). The graph below illustrates the area under the product curve of the wavelet and the signal. The algebraic sum of the contributing areas, each linked to wavelet lobes, corresponds to the indicator value yielded by the WT (after taking the ratio c/d for IDrop). Computations are presented for the year 2008.

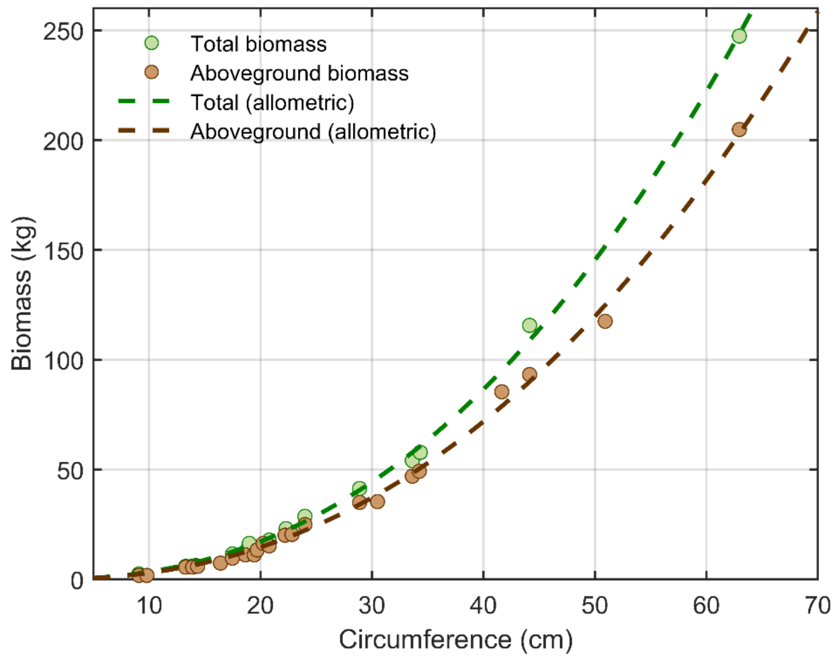

Figure S2: Allometric relationships used to estimate tree biomass at FR-Hes. Total biomass (green dashed line) and aboveground biomass (brown dashed line) are shown as a function of tree circumference, together with observed data points. The relationships follow power-law formulations calibrated from destructive sampling (Ottorini, 2012, unpublished dataset). The figure is adapted from original material provided by J. M. Ottorini. Model parameters are highly significant for both relationships ($p < 0.001$), supporting their use for biomass estimation across the study period.

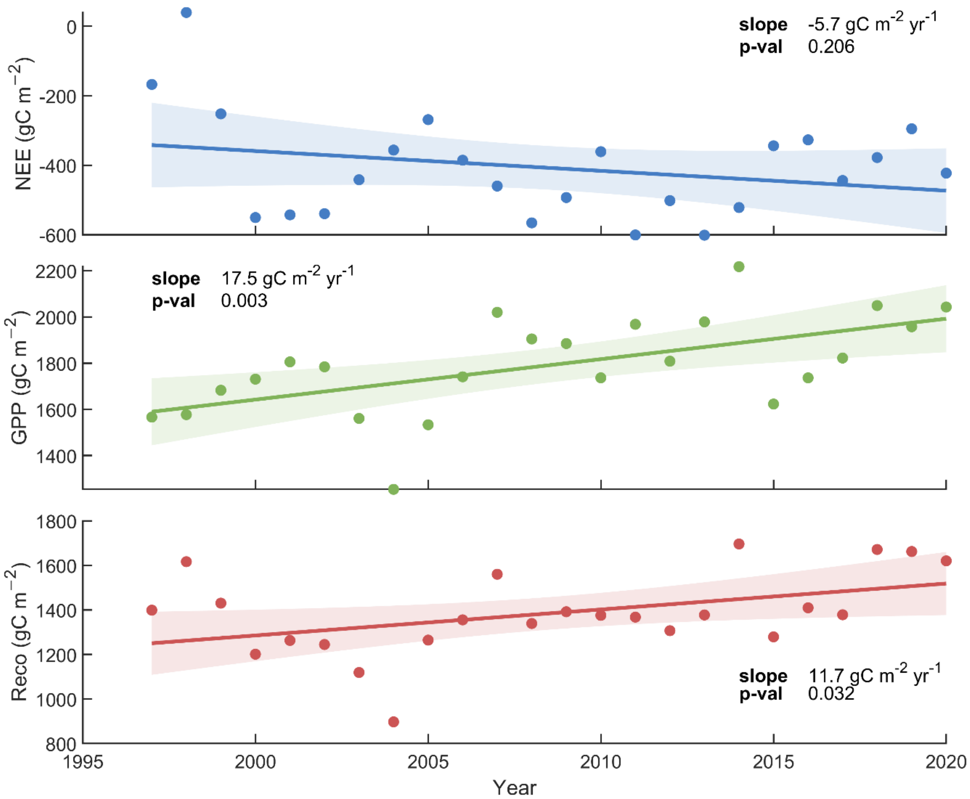

Figure S3: Interannual variability of annual net ecosystem exchange (NEE), gross primary production (GPP), and ecosystem respiration (Reco) from 1997 to 2020. Dots represent annual values and solid lines show linear trends fitted using ordinary least squares. Shaded areas indicate 95 % confidence intervals around the trend. For each flux, the estimated slope of the linear regression and its associated *p*-value are reported.

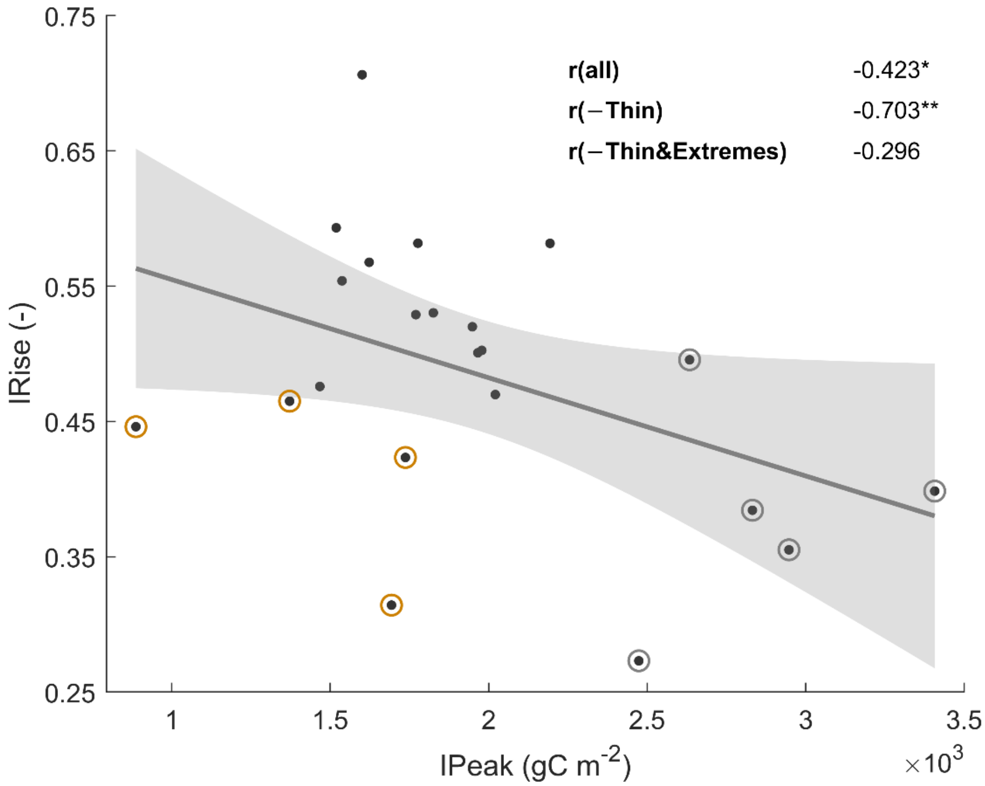

Figure S4: Scatter plot showing the relationship between IRise and IPeak. Thinning years are highlighted with yellow circles and extreme-summer years with grey circles. Correlation coefficients are reported for (1) the full time series, (2) the subset excluding thinning years, and (3) the subset excluding both thinning and extreme-summer years. Statistical significance is indicated by one, two, or three stars for $p \leq 0.05$, 0.01, and 0.001, respectively. Indicators represent wavelet-derived metrics and should be interpreted comparatively.

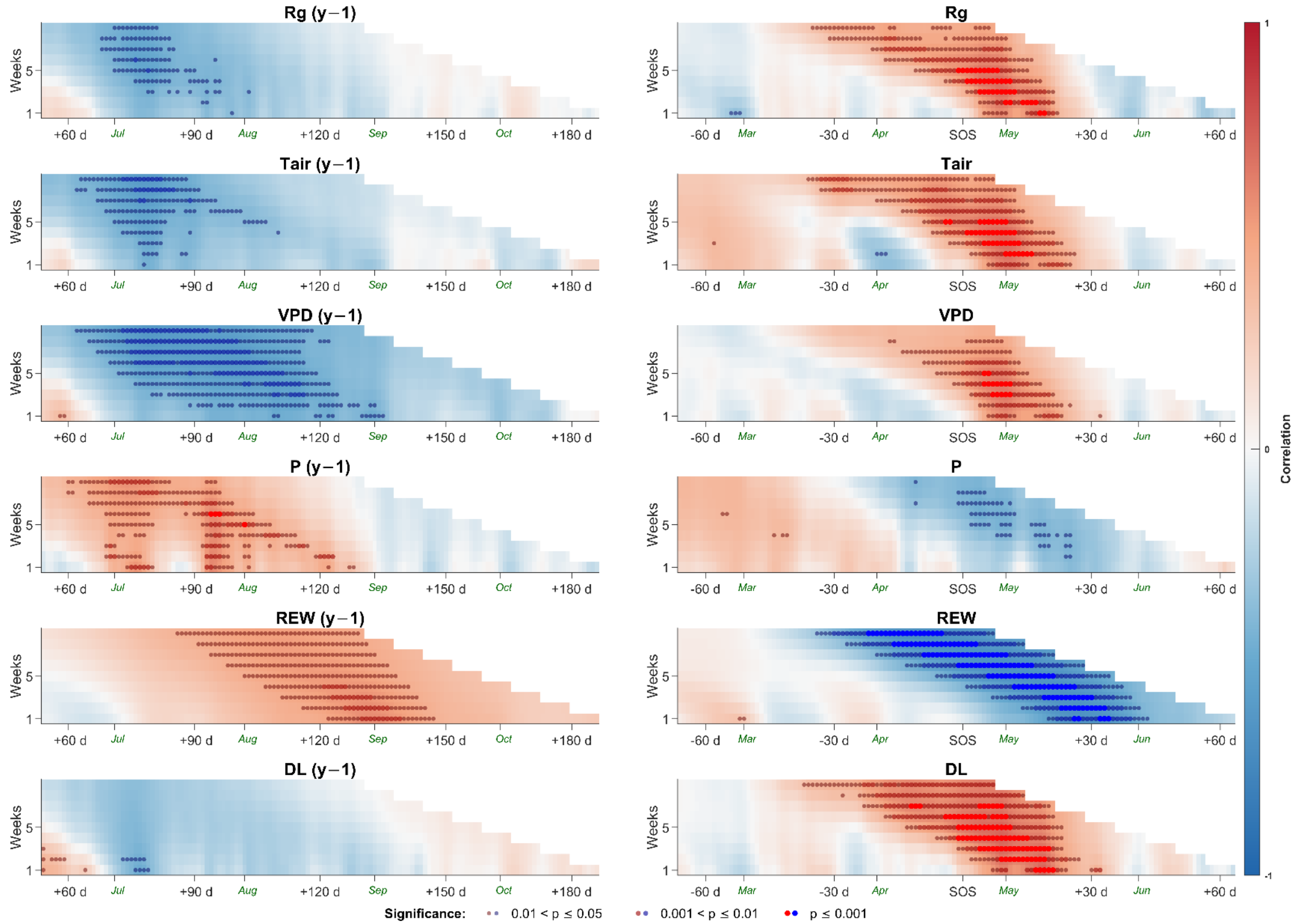

Figure S5: Correlograms depicting sliding-window Pearson correlations between IRise and environmental drivers averaged over different window sizes (*y*-axis, in weeks) and starting dates (*x*-axis, in days relative to SOS). Average calendar dates (across all years) at which each month begins are indicated in green. Correlations were computed on a 1 week × 1 d grid and lightly smoothed using an anisotropic Gaussian filter ($\sigma_x = 0.8$ d, $\sigma_y = 1.3$ d) for clarity. Statistical significance, computed on the unsmoothed correlations, is represented by markers whose size, opacity, and color saturation scale with *p*-value. Colors indicate correlation sign and magnitude (red = positive; blue = negative). Left panels represent previous-year effects and right panels current-year effects.

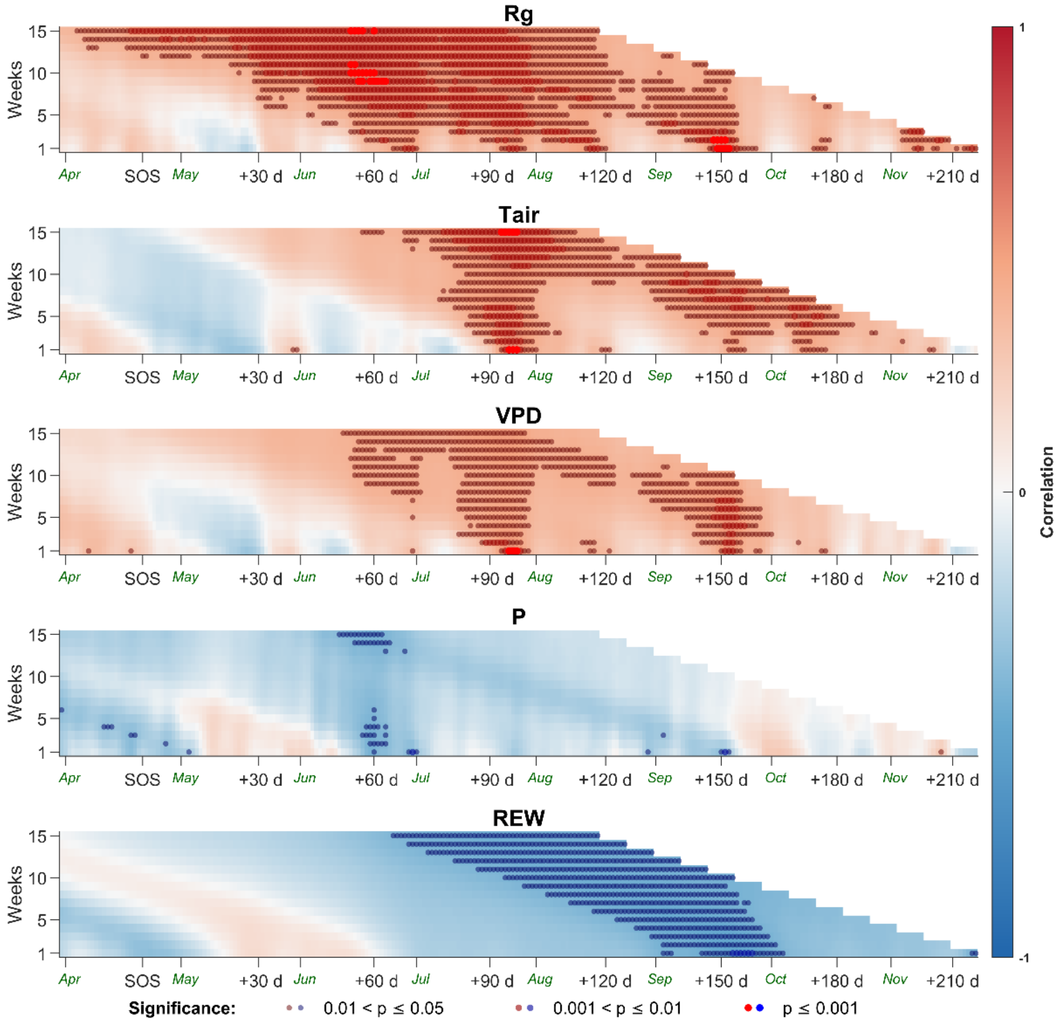

Figure S6: Correlogram depicting sliding-window Pearson correlations between IPeak and current-year environmental drivers. For methodological details and full description of correlogram structure, see Fig. S5.

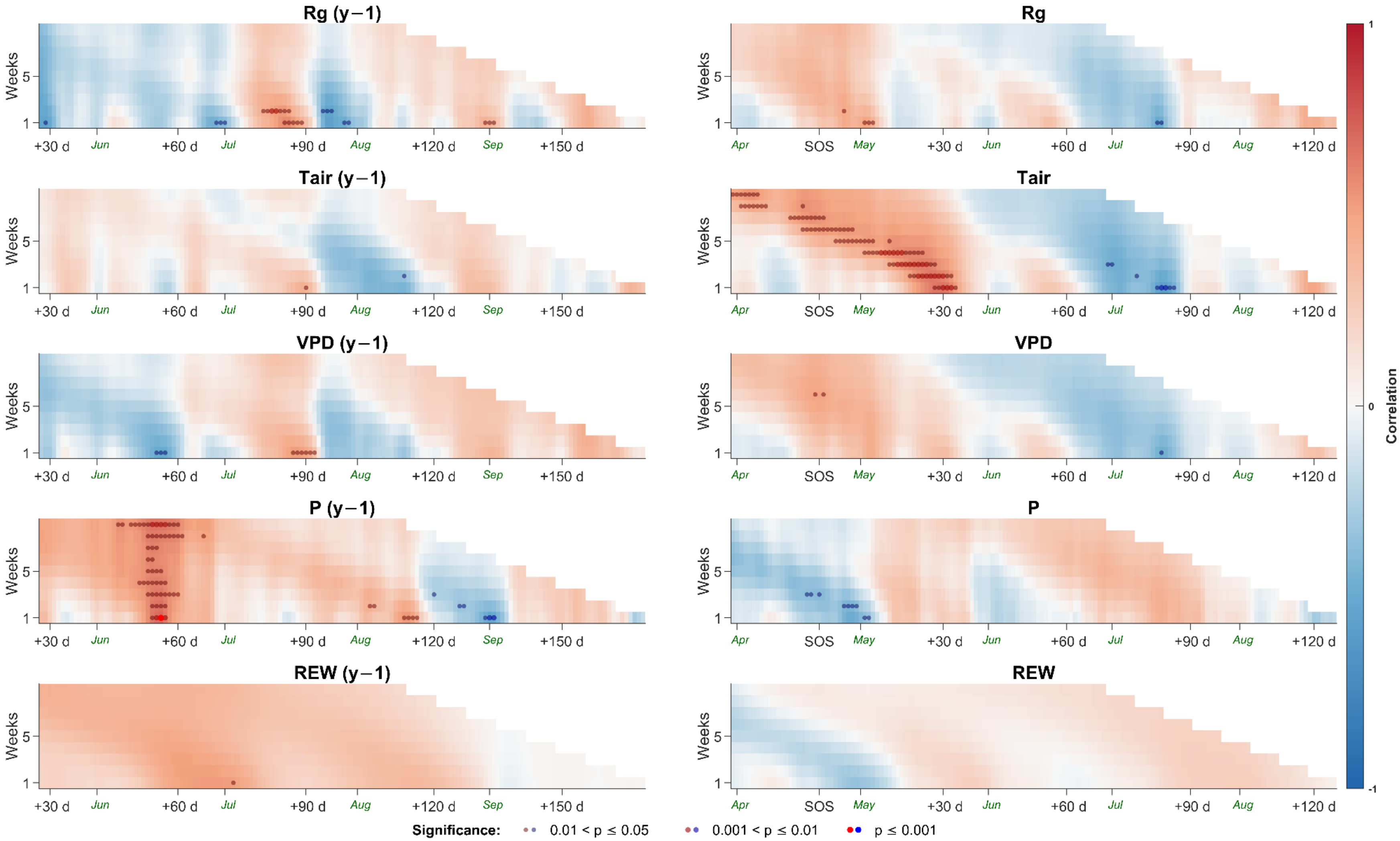

Figure S7: Correlogram depicting sliding-window Pearson correlations between IPeak and environmental drivers, excluding thinning (1999, 2005, 2010, 2016) and extreme summer (2013, 2014, 2018, 2019, 2020) years. For methodological details and full description of correlogram structure, see Fig. S5.

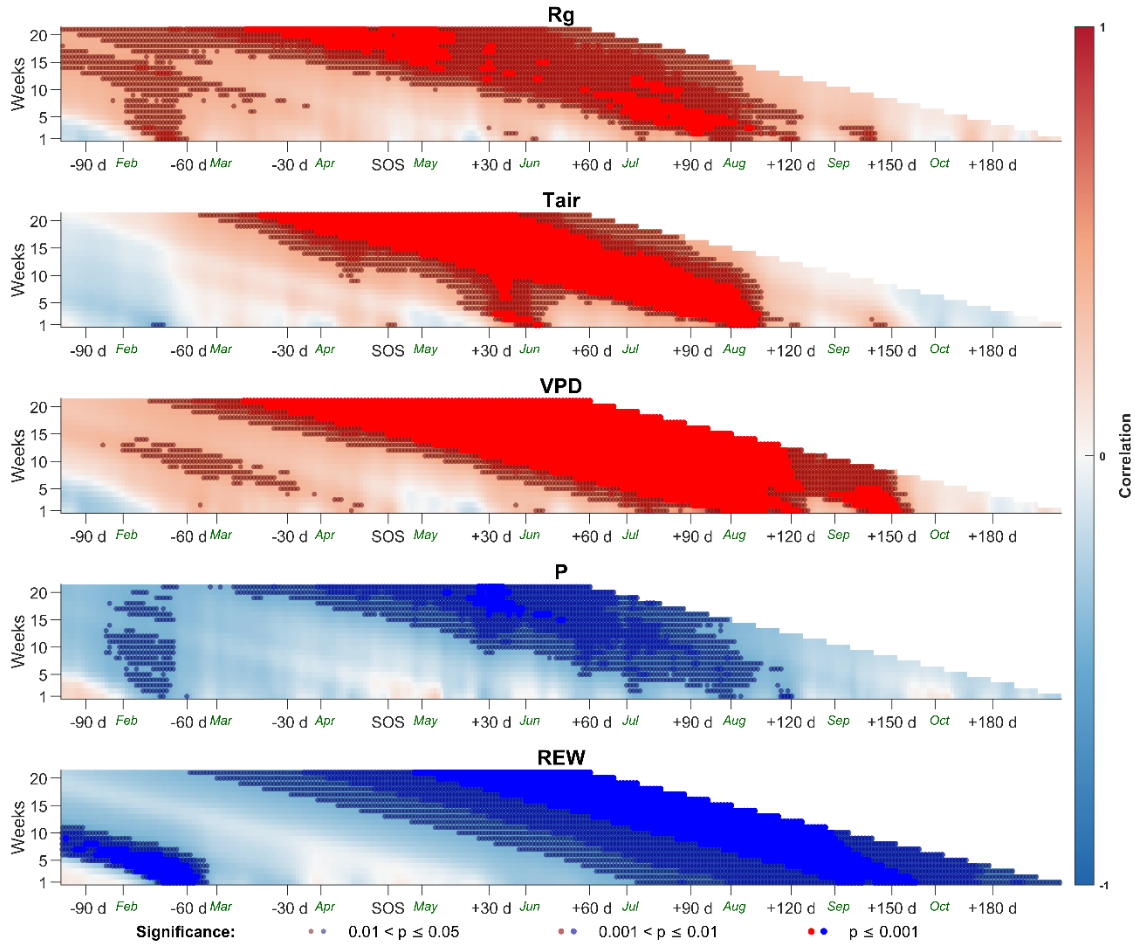

Figure S8: Correlogram depicting sliding-window Pearson correlations between IDrop and current-year environmental drivers. For methodological details and full description of correlogram structure, see Fig. S5.

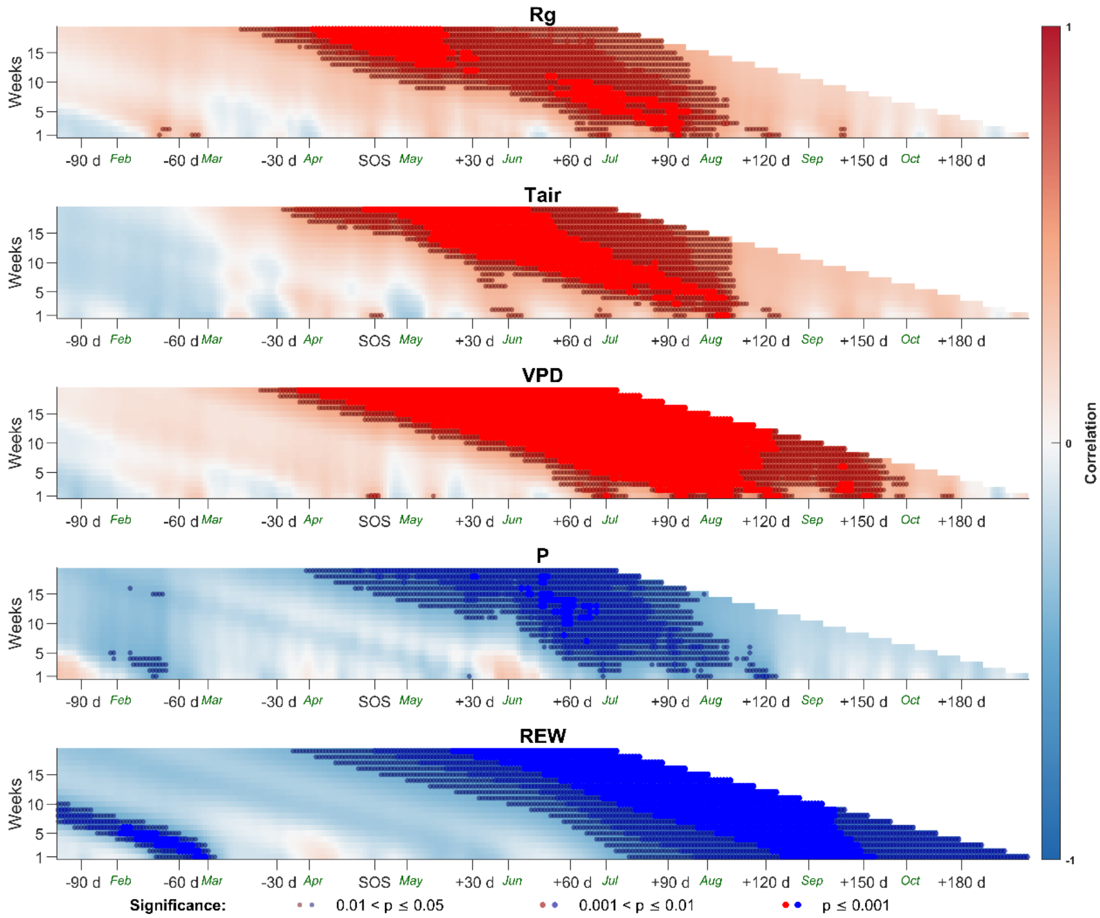

Figure S9: Correlogram depicting sliding-window Pearson correlations between IDrop and current-year environmental drivers, excluding the exceptional 2003 drought year. For methodological details and full description of correlogram structure, see Fig. S5.

Table S1: Significant correlations extracted from the IRise correlogram (Fig. S5), separated according to previous-year and current-year influences. For each correlation group, variables selected through partial correlation analysis are shown in blue. Window start and end dates are expressed in days relative to SOS. Correlation coefficients are listed in the rightmost column of each section, with statistical significance indicated by one, two, or three stars for $p \leq 0.05$, 0.01 and 0.001, respectively. The first section summarizes long-scale correlations, followed by shorter-scale correlation windows organized according to their temporal proximity. The number of data points (n) used to estimate correlations is indicated in parentheses.

Previous year (n = 21)				
	Variable	Start	End	Correlation
Long-scale	**P_{y-1}**	+95	+137	0.693***
	VPD_{y-1}	+99	+141	−0.639**
	$Tair_{y-1}$	+78	+141	−0.627**
	REW_{y-1}	+134	+141	0.604**
	Rg_{y-1}	+76	+118	−0.556**
Short-scale	**P_{y-1}**	+77	+84	0.649**
	P_{y-1}	+94	+115	0.638**
	P_{y-1}	+120	+134	0.623**

Current year (n = 22)				
	Variable	Start	End	Correlation
Long-scale	**Rg**	+10	+31	0.782***
	Tair	+10	+31	0.774***
	DL	+10	+38	0.765***
	VPD	+10	+31	0.712***
	REW	+9	+51	−0.709***
	P	+4	+46	−0.508*
Short-scale (1st part)	**Tair**	+10	+17	0.602**
	DL	+9	+16	0.583**
	VPD	+9	+16	0.559**
	Rg	+9	+16	0.537*
Short-scale (2nd part)	DL	+18	+25	0.763***
	Rg	+15	+29	0.741***
	Tair	+16	+30	0.652***
	VPD	+20	+27	0.635**

Table S2: Significant correlations extracted from the IPeak correlogram (Fig. S6). For a description of variables, window definitions and methodological notes, see Table S1.

Current year (n = 22)				
	Variable	Start	End	Correlation
Long-scale	**Rg**	+55	+125	0.673***
	Tair	+95	+200	0.668***
Short-scale (1st part)	**Rg**	+70	+77	0.619**
	P	+70	+77	−0.584**
	VPD	+70	+77	0.45*
Short-scale (2nd part)	**VPD**	+96	+103	0.789***
	Tair	+96	+103	0.712***
	Rg	+97	+104	0.593**
Short-scale (3rd part)	**Rg**	+151	+158	0.743***
	VPD	+153	+181	0.595**
	Tair	+153	+202	0.58**
	P	+151	+158	−0.55**
	REW	+154	+161	−0.542**

Table S3: Significant correlations extracted from the IPeak correlogram excluding thinning and extreme summer years (Fig. S7). For a description of variables, window definitions and methodological notes, see Table S1.

Previous year (n = 12)				
	Variable	Start	End	Correlation
Long-scale	**P_{y-1}**	+57	+120	0.716**
Short-scale	**P_{y-1}**	+56	+63	0.828***
	VPD_{y-1}	+56	+63	−0.636*

Current year (n = 13)				
	Variable	Start	End	Correlation
Long- & short-scale	**Tair**	+22	+43	0.785**
	Rg	+12	+19	0.668*
	P	−33	+23	−0.64*
	VPD	+1	+43	0.574*

Table S4: Significant correlations extracted from the IDrop correlogram (Fig. S8), organized into two groups based on temporal proximity. For a description of variables, window definitions and methodological notes, see Table S1.

*Current year – **1st group (n** = 21)*				
	Variable	Start	End	Correlation
Long-scale	Rg	+86	+128	0.769***
	Tair	+33	+131	0.899***
	VPD	+50	+162	0.932***
	P	+31	+157	−0.725***
	REW	+60	+207	−0.745***
Short-scale (1st part)	**Tair**	+39	+53	0.775***
Short-scale (2nd part)	**Rg**	+91	+112	0.748***
	P	+92	+113	−0.549*
Short-scale (3rd part)	**VPD**	+107	+114	0.932***
	Tair	+107	+114	0.856***

*Current year – **2nd group (n = 21)***				
	Variable	Start	End	Correlation
Long- & short-scale	**REW**	−70	−42	−0.83***
	P	−67	−53	−0.538*
	Rg	−66	−59	0.648**

Table S5: Significant correlations extracted from the IDrop correlogram excluding the 2003 drought year (Fig. S9), organized into two groups based on temporal proximity. For a description of variables, window definitions and methodological notes, see Table S1.

*Current year – **1st group (n = 20)***				
	Variable	Start	End	Correlation
Long-scale	Rg	+8	+113	0.789***
	Tair	+32	+137	0.834***
	VPD	+53	+186	0.914***
	P	+58	+142	−0.736***
	REW	+81	+207	−0.799***
	VPD	+92	+134	0.911***
Short-scale (1st part)	**VPD**	+71	+78	0.685***
	Rg	+70	+77	0.594**
	P	+70	+84	−0.57**
	Tair	+70	+77	0.507*
Short-scale (2nd part)	**Rg**	+92	+106	0.827***
	VPD	+92	+106	0.779***
	P	+92	+113	−0.588**
Short-scale (3rd part)	**VPD**	+107	+114	0.822***
	Tair	+107	+114	0.781***
Short-scale (4th part)	**VPD**	+121	+128	0.78***
	P	+119	+126	−0.627**
	Rg	+121	+128	0.564**
	Tair	+122	+129	0.484*
Short-scale (5th part)	VPD	+144	+158	0.765***
	REW	+138	+145	−0.756***
	Rg	+143	+157	0.524*

*Current year – **2nd group (n** = 20)*				
	Variable	Start	End	Correlation
Long- & short-scale	**REW**	−70	−42	−0.782***
	P	−67	−46	−0.549*
	Rg	−65	−51	0.466*